

## ARTICLES

## Effect of Particle Size on Melting of Aluminum at Nano Scales

Puneesh Puri and Vigor Yang\*

*The Pennsylvania State University, University Park, Pennsylvania 16802**Received: March 29, 2007; In Final Form: May 24, 2007*

Molecular-dynamics simulations are performed using isobaric–isoenthalpic (NPH) ensembles to predict the melting of nanosized aluminum particles in the range of 2–9 nm and to investigate the effect of surface charge development on the melting. Five different potential functions (the Lennard-Jones, glue, embedded-atom, Streitz–Mintmire, and Sutton–Chen potentials) are implemented, and the results are evaluated using the particle-size dependence of the melting phenomenon as a benchmark. A combination of structural and thermodynamic parameters, including the potential energy, Lindemann index, translational-order parameter, and radial-distribution functions, are used to characterize the melting process. Both bulk and particle melting are considered. The former features sharp changes in structural and thermodynamic properties across the melting point, as opposed to the smooth variations seen in particle melting in which surface premelting plays an important role. The melting temperature of a nanoparticle increases monotonically with increasing size, from 473 K at 2 nm to a bulk value of 937 K at approximately 8 nm. Two-body potentials like the Lennard-Jones potential fail to predict the thermodynamic melting phenomenon. The Sutton–Chen potential, fitted to match structural properties, also fails to capture the size dependence of particle melting. The many-body glue and Streitz–Mintmire potentials accurately predict melting temperature as a function of particle size. The effect of surface charges on melting is found to be insignificant for nanosized aluminum particles.

## I. Introduction

Nanosized aluminum and other metallic particles have been extensively used in many propulsion and energy-conversion applications due to their unusual energetic properties, such as increased catalytic activity and higher reactivity.<sup>1–2</sup> The excess energy of surface atoms and reduced activation energies for chemical reactions contribute to these extraordinary chemical characteristics.<sup>3</sup>

At nanoscales, particles exhibit many thermo-physical features distinct from those found at microscales. As the size decreases beyond a critical value, due to the increase in the surface-to-volume ratio, the melting temperature deviates from the bulk value and becomes a size-dependent property.<sup>4</sup> This phenomenon has been studied experimentally by means of transmission electron diffraction by Wronski for nanosized tin.<sup>5</sup> The apparatus consists of an evaporator attached to a small furnace, and 5–10 nm particles are produced by evaporating a tin pellet from the surface and then condensing it on a thin carbon or silicon monoxide substrate. The melting points agree reasonably well with the predictions based on classical theories, which show a nonlinear relationship with the reciprocal of the particle size. The melting temperature of tin becomes size-dependent for particles smaller than 10 nm, reducing from a bulk value of 505 to 425 K for a 5 nm particle. Eckert et al. synthesized nanocrystalline aluminum powders by mechanical attrition in argon, hydrogen, and oxygen atmospheres and observed a similar reduction in the melting point with decreasing grain size.<sup>6</sup> The study was performed for 13–40 nm particles using differential scanning calorimetry (DSC). The melting point

increases from 840 K for 13 nm particles, and reaches its bulk value of 940 K for 40 nm particles. In addition to these experimental studies, Alavi et al.<sup>4</sup> performed molecular-dynamics simulations for clusters of aluminum atoms using the Streitz–Mintmire potential and canonical (NVT) ensembles. Special attention was given to the structure of the cluster and dynamic coexistence of the liquid and solid phases. However, only clusters up to a size of 3 nm (i.e., 1000 atoms) were considered.

Particle size plays a significant role in determining the characteristics of ignition and combustion. For micron-sized and larger aluminum particles, the ignition temperature coincides with the melting point of the surface oxide ( $\text{Al}_2\text{O}_3$ ) layer at 2327 K.<sup>7</sup> The impervious nature of aluminum oxide inhibits the ignition of aluminum. Once the layer melts, it coalesces to form an oxide cap, and the aluminum core is then exposed to the ambient gases for oxidation. At nano scales (less than 100 nm), the ignition occurs near the melting point of aluminum at 940 K by cracking of the oxide shell, possibly caused by the pressure buildup<sup>8,9</sup> and/or phase transformations<sup>10,11</sup> inside the shell. According to Rai et al.,<sup>8</sup> oxidation of alumina-coated nanosized aluminum particles is initiated by melting of the aluminum core. The resultant volume dilatation causes a pressure build-up inside the shell formed by the oxide layer. Because of the higher curvature as compared to micron-sized particles, the stress developed due to the pressure becomes unsustainable, and the shell subsequently ruptures. This concept was originally introduced by Rozenband et al.,<sup>9</sup> who developed a model taking into account the mechanical stresses at the metal–oxide interface.<sup>9</sup> Trunov et al.<sup>11</sup> attributed the observed low ignition temperature of nanosized particles to the transformation from the amorphous to the gamma and alpha phases in the oxide layer. As a

\* Corresponding author. E-mail: vigor@psu.edu. Phone: (814) 863-1502. Fax: (814) 865-3389.

consequence of the density variations in different phases, the layer develops cracks, which permit direct oxidation of aluminum in the core. Campbell et al.<sup>12</sup> conducted molecular-dynamics simulations for the oxidation of a 20 nm aluminum particle. The effect of particle size on the melting and ignition of aluminum was not addressed.

In light of the inconsistency and uncertainties of the various theories concerning the particle behavior at nano scales,<sup>8–11</sup> fundamental research based on well-calibrated techniques appears to be imperative, in order to achieve an improved understanding of the effects of particle size on the melting and ignition behavior. The purpose of the present work is to perform a molecular-dynamics study of the melting of aluminum particles in the size range of 2–9 nm consisting of 256–23328 atoms. The influence of the surface passivating layer is not considered, but will be treated in subsequent work. Results will not only provide basic information about particle behavior at nano scales, but will also set the stage for a study of the ignition and combustion of aluminum particles over a broad range of scales.

Another objective of this work is to select an optimum potential that can accurately and efficiently predict the melting of nanoscale aluminum particles. Five existing potentials (the Lennard-Jones, glue, embedded-atom, Streitz–Mintmire, and Sutton–Chen potentials) are implemented and evaluated. The resultant melting process is characterized using a combination of structural and thermodynamic parameters, including the potential energy, Lindemann index, translational-order parameter, and radial-distribution functions. Both bulk material and nanoparticles are considered. The dynamic coexistence of the solid and liquid phases is also explored. In addition, the effect of surface charge development on melting is examined using the Streitz–Mintmire potential.

## II. Theoretical and Computational Framework

Isobaric–isoenthalpic (NPH) ensemble is employed in the present study of melting of nanosized aluminum particles. A system of  $N$  atoms is coupled to an external source by introducing additional variables into the Lagrangian. NPH ensemble was first introduced by Anderson<sup>13</sup> using volume as an extra degree of freedom through mechanical coupling. Assuming that atoms behave as classical point-like masses, the Lagrangian of the system is expressed as

$$L = \sum_i \frac{mV^{2/3}\dot{d}_i^2}{2} + \frac{M\dot{V}^2}{2} - U(V^{1/3}d_1, \dots, V^{1/3}d_{3N}) - PV \quad (1)$$

where  $M$  is a constant fictitious mass associated with the volume of the system,  $m$  is the mass of the atom,  $V$  is the volume, treated as a dynamic variable,  $P$  is the pressure, and  $d_i$  is the scaled position of atom  $i$ . The Lagrangian equations of motion can be written as

$$\frac{d}{dt} \frac{\partial L}{\partial \dot{q}_i} = \frac{\partial L}{\partial q_i} \quad (2)$$

where  $q_i$  are generalized coordinates. When  $q_i$  is substituted for  $V$  and  $d_i$  in eq 2, the equations of motion for the case of NPH ensemble take the form

$$\begin{aligned} M\ddot{V} &= -P + \frac{1}{3V} [V^{2/3} \sum_i m_i \dot{d}_i^2 - V^{1/3} \sum_i F_i d_i] \\ m_i \ddot{d}_i &= V^{-1/3} F_i - \frac{2m_i \dot{V} \dot{d}_i}{3V} \end{aligned} \quad (3)$$

where  $\dot{d}_i$  and  $\ddot{d}_i$  denote the first-order and second-order derivatives with respect to time, and  $F_i$  is the net force on atom  $i$ . Equation 3 is numerically integrated using a fifth-order predictor-corrector algorithm.<sup>13</sup> The time step is chosen to be one femtosecond, considering that the time scale for vibration of atoms is of the same order. Annealing is achieved using the velocity scaling, and the temperature of the nanoparticle is increased at a rate of 0.01 K per time step. A parametric study was performed on a bulk FCC crystal consisting of 2048 atoms with different temperature rises of 1, 0.1, 0.01, and 0.001 K per femtosecond for each time step. A rate lower than 0.01 K/step increases the total computational time, and a higher rate gives insufficient time for particles to equilibrate at each step leading to erroneous results. An optimum rate of 0.01 K/step also helps in accurately predicting the melting point because it produces better resolution in the variations of thermodynamic and structural properties.

The macroscopic thermodynamic properties of the system are derived from the instantaneous values using the equation of state and statistical mechanics. For example, the temperature can be determined from the kinetic energy of atoms according to the equipartition principle

$$T = \frac{2\langle K \rangle}{3Nk_B} \quad (4)$$

For any physical property  $A$ ,  $\langle A \rangle$  denotes an average over time given by<sup>14</sup>

$$\langle A \rangle = \frac{1}{N_{\text{step}}} \sum_{i=1}^{N_{\text{step}}} A(\Gamma_i) \quad (5)$$

where  $\Gamma_i$  represents a  $6N$ -dimensional phase space consisting of positions and momenta of all atoms. The pressure is calculated through the virial equation of state, as a function of the temperature of the system and forces experienced by all of the atoms

$$P = Nk_B T + \left\langle \frac{1}{3} \sum_{i=1}^N r_i \cdot F_i \right\rangle \quad (6)$$

The melting point is identified based on the variations in the potential energy, Lindemann index, and translational order parameter. The Lindemann index, defined as<sup>15</sup>

$$\delta = \frac{2}{N(N-1)} \sum_{i < j} \frac{\sqrt{\langle r_{ij}^2 \rangle_t - \langle r_i \rangle_t^2}}{\langle r_{ij} \rangle_t} \quad (7)$$

measures the vibrational motion of atoms and can be calculated as a function of interatomic distance. The increase in vibrational motion is a characteristic of the phase change in materials, and the Lindemann index is expected to increase abruptly by a factor of more than three during melting. The translational-order parameter,  $\lambda$ , is a measure of the structure present in the solid, expressed as<sup>16</sup>

$$\begin{aligned} \lambda &= \frac{1}{N} \sqrt{\left( \sum_{i=1}^N \cos(k \cdot r_i) \right)^2 + \left( \sum_{i=1}^N \sin(k \cdot r_i) \right)^2} \\ k &= \left( \frac{(2N)^{1/3} \pi}{L} \right) (-1, 1, 1) \end{aligned} \quad (8)$$

where  $k$  is an arbitrary vector of the lattice and  $L$  is the side

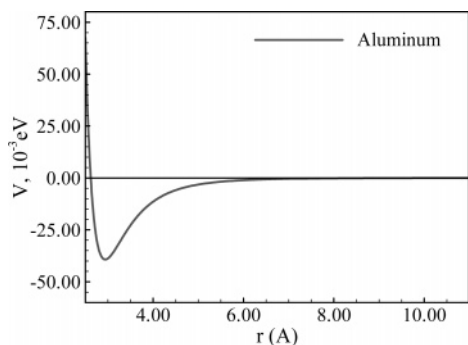


**Figure 1.** Lennard-Jones potential for aluminum.

length of the simulation domain. In a solid, atoms simply vibrate about their lattice positions, and hence, there is perfect order in the crystal. Such order, however, disappears in a liquid state, and the corresponding translational-order parameter is reduced by an order of magnitude.

The general computational framework developed in the current molecular-dynamics study can handle microcanonical (NVE), isobaric–isoenthalpic (NPH), and isobaric–isothermal (NPT) ensembles using both Verlet and predictor–corrector algorithms.<sup>14</sup> These algorithms have been parallelized using the atomic decomposition method.<sup>17</sup> A separate postprocessing code has also been developed to superimpose the grid on the geometry under consideration and to analyze the results using the contours of various thermodynamic properties. The code has the capability of handling multiatom simulations and can treat liquid and solid phases.

### III. Potentials

According to the Born–Oppenheimer approximation, the nuclear and electronic motions in molecules can be separated and the nuclear motion sees a smeared-out potential from the speedy electrons. The potential functions are an approximation to this potential energy surface, and are fitted to such experimental data as structural, thermodynamic or material properties. Moreover, almost all of the potentials considered are fitted to the properties for bulk materials.

Five commonly used potential functions (the Lennard-Jones, glue, embedded-atom, Sutton–Chen, and Streitz–Mintmire potentials) are employed in the present study. All but the Lennard-Jones potential are many-body potentials. Among the five potentials, only the Streitz–Mintmire potential is capable of handling both aluminum and aluminum oxide.<sup>18</sup> The Lennard-Jones potential is defined as

$$V_{\text{LJ}}(r) = 4\epsilon_{\text{LJ}}[(\sigma_{\text{LJ}}/r)^{12} - (\sigma_{\text{LJ}}/r)^6] \quad (9)$$

where  $\epsilon_{\text{LJ}}$  and  $\sigma$  are the empirical parameters accounting for the depth of the potential well and the distance between two atoms at which the potential is zero, respectively. Their specific values of  $\epsilon/k_{\text{B}} = 4551$  K and  $\sigma = 2.62$  Å were provided by Halicioglu et al.<sup>19</sup> based on the physical properties (such as lattice constants, heat capacity, and thermal expansion constant) for crystalline-state aluminum. Figure 1 shows the variation of the potential as a function of the distance between atoms.

The glue potential is defined by a pair potential  $\varphi(r)$ , an atomic density function  $\rho(r)$ , and a glue function  $U(\rho)$ . Ercollessi et al.<sup>20</sup> presented a scheme to extract numerically optimal interatomic glue potentials from the results produced by first-principle calculations involving electronic structures. The method is based on fitting the potential to ab initio atomic forces of diverse atomic configurations including surfaces, clusters,

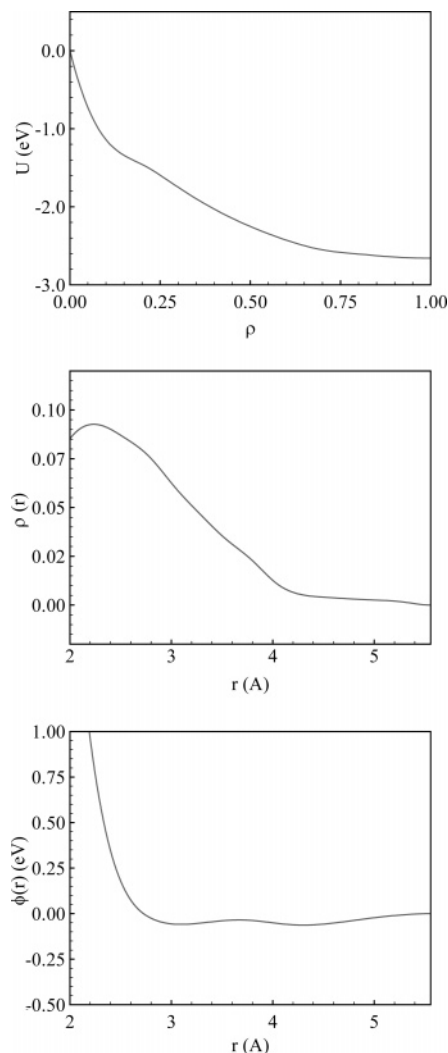


**Figure 2.** Glue potential for aluminum.

liquids, and crystals at different temperatures. Figure 2 shows the three functions constituting the optimized glue potential for aluminum. The functional form for the glue potential is

$$V_{\text{glue}} = \frac{1}{2} \sum_{ij} \varphi(r_{ij}) + \sum_i U(\sum_j \rho(r_{ij})) \quad (10)$$

The difference between the two-body Lennard-Jones and the many-body glue potential can be analyzed by comparing Figures 1 and 2. In the Lennard-Jones potential, the potential energy surface is represented using a single expression which captures both attractive and repulsive forces between two atoms as a function of their separation. The glue potential, however, consists of two functions. The first function  $\varphi(r_{ij})$  bears a close resemblance to the Lennard-Jones potential and captures repulsive forces when the separation between atoms is small. The second part,  $U(\rho)$ , known as the glue function, characterizes the effect of atomic density on the forces between two atoms. Since metals feature strong cohesive forces, many-body potentials can be more effective in predicting metal properties accurately than the Lennard-Jones potential.

The Sutton–Chen potential extends the empirical  $N$ -body potentials, originally developed by Finnis and Sinclair for description of cohesion in metals,<sup>21</sup> to include a long-range modification using the van der Waals tail.<sup>22</sup> This potential takes the form

$$V_{\text{SC}} = \epsilon_{\text{SC}} \left[ \frac{1}{2} \sum_i \sum_{j \neq i} V(r_{ij}) - c \sum_i \sqrt{\rho_i} \right]$$

$$V(r_{ij}) = (a/r_{ij})^7; \quad \rho_i = \sum_{j \neq i} (a/r_{ij})^6 \quad (11)$$

The constants  $\epsilon$ ,  $c$ , and  $a$  have values of 0.033147 eV, 16.399, and 4.05 Å respectively. The functional form is similar to the glue potential because of the presence of pair potentials and atomic-density-dependent terms.

The Streitz–Mintmire potential<sup>18</sup> has the same functional form as the glue and Sutton–Chen potentials but includes electrostatic forces due to charges on atoms. It consists of two parts: an embedded-atom part and an electrostatic part accounting for charges on atoms. The embedded-atom potential used in the current study is a modification of the Streitz–Mintmire potential, consisting of only the embedded-atom part of the complete potential. The electrostatic part and associated charge development are not considered. The embedded-atom part of the potential is defined as

$$V_{\text{EAM}} = \sum_i F_i[\rho_i] + \sum_{i < j} \varphi_{ij}(r_{ij})$$

$$\rho_i(r) = \sum_{j \neq i} \xi_j e^{-\beta_j(r_{ij} - r_{ij}^*)}$$

$$F_i(\rho_i) = -A_i \sqrt{\frac{\rho_i}{\xi_i}}$$

$$\varphi_{ij}(r) = 2B_{ij} e^{-\beta_{ij} 2(r - r_{ij}^*)} - C_{ij} [1 + \alpha(r - r_{ij}^*)] e^{-\alpha(r - r_{ij}^*)} \quad (12)$$

where  $F_i(\rho_i)$  represents the energy required to embed atom  $i$  in electron density  $\rho_i$ , and  $\varphi_{ij}(r)$  is the pairwise interaction. The parameters used in the above functional forms for aluminum are<sup>18</sup>

$$\xi_{\text{Al}} = 0.147699; \quad \xi_{\text{O}} = 1.0$$

$$r_{\text{Al-Al}}^* = 3.365875 \text{ Å}; \quad r_{\text{Al-O}}^* = 2.358570 \text{ Å}; \quad r_{\text{O-O}}^* = 2.005092 \text{ Å}$$

$$\beta_{\text{Al-Al}} = 2.017519 \text{ Å}^{-1}; \quad \beta_{\text{Al-O}} = 4.507976 \text{ Å}^{-1}; \quad \beta_{\text{O-O}} = 6.871329 \text{ Å}^{-1}$$

$$A_{\text{Al}} = 0.763905 \text{ eV}; \quad A_{\text{O}} = 2.116850 \text{ eV}$$

$$B_{\text{Al-Al}} = 0.075016 \text{ eV}; \quad B_{\text{Al-O}} = 0.154548 \text{ eV}; \quad B_{\text{O-O}} = 1.693145 \text{ eV}$$

$$C_{\text{Al-Al}} = 0.159472 \text{ eV}; \quad C_{\text{Al-O}} = 0.094594 \text{ eV}; \quad C_{\text{O-O}} = 1.865072 \text{ eV}$$

$$\alpha_{\text{Al-Al}} = 1.767488 \text{ Å}^{-1}; \quad \alpha_{\text{Al-O}} = 4.233670 \text{ Å}^{-1}; \quad \alpha_{\text{O-O}} = 8.389842 \text{ Å}^{-1} \quad (13)$$

The pair potential, as also seen in other potentials, becomes strongly repulsive at smaller distances. The electrostatic part is given by<sup>18</sup>

$$V_{\text{ES}} = \sum_i v_i(q_i) + \frac{1}{2} v_{ij}(r_{ij}; q_i; q_j)$$

$$v_i(q_i) = v_i(0) + \chi_i^0 q_i + \frac{1}{2} J_i^0 q_i^2$$

$$v_{ij}(r_{ij}; q_i; q_j) = \int d^3 r_1 \int d^3 r_2 \rho_i(r_1; q_i) \rho_j(r_2; q_j) / r_{12} \quad (14)$$

where  $v_i(q_i)$  is the local atomic energy,  $\chi_i^0$  is the electro negativity, and  $J_i^0$  is the second derivative associated with the self-Coulomb repulsion.  $v_{ij}(r_{ij}; q_i; q_j)$  denotes the electrostatic interaction energy between atoms  $i$  and  $j$ . The charge density distribution,  $\rho_i(r; q_i)$ , for a Slater 1s orbital about atom  $i$  for a charge  $q_i$ , is defined as

$$\rho_i(r; q_i) = Z_i \delta(r - r_i) + (q_i - Z_i) \left( \frac{\xi_i^3}{\pi} \right) e^{-2\xi_i |r - r_i|} \quad (15)$$

where  $\xi_i$  is the decay length for the atomic orbital, and  $Z_i$  the effective core charge. Further simplification of the interaction energy using an analytical expression for Coulomb integrals<sup>23</sup> yields

$$V_{\text{ES}} = \sum_i q_i [\chi_i^0 + \sum_{j \neq i} Z_j (\omega_i(r_{ij}) - v_{ij}(r_{ij}))] + \frac{1}{2} \sum_i q_i^2 J_i^0 + \frac{1}{2} \sum_{j \neq i} q_i q_j \left( \frac{1}{r_{ij}} + v_{ij}(r_{ij}) \right)$$

$$v_{ij}(r) = -\frac{(1 - \kappa)^2}{4r} (2 + \kappa + \xi_i r) e^{-2\xi_i r} - \frac{(1 + \kappa)^2}{4r} (2 - \kappa + \xi_j r) e^{-2\xi_j r} \quad \text{for } \xi_i \neq \xi_j$$

$$v_{ij}(r) = -\left\{ 1 + \frac{11}{8} \xi_i r + \frac{3}{4} (\xi_i r)^2 + \frac{1}{6} (\xi_i r)^3 \right\} \frac{e^{-2\xi_i r}}{r} \quad \text{for } \xi_i = \xi_j$$

$$\omega_j(r) = -\frac{1 + \xi_j r}{r} e^{-2\xi_j r}$$

$$\kappa = (\xi_i^2 + \xi_j^2) / (\xi_i^2 - \xi_j^2) \quad (16)$$

The constants in the above integrals are given by<sup>18</sup>

$$\chi_{\text{Al}}^0 = 0.0 \text{ eV}; \quad \chi_{\text{O}}^0 = 5.484763 \text{ eV}$$

$$Z_{\text{Al}} = 0.746759; \quad Z_{\text{O}} = 0.0$$

$$J_{\text{Al}}^0 = 10.328655 \text{ eV}; \quad J_{\text{O}}^0 = 14.035715 \text{ eV}$$

$$\xi_{\text{Al}} = 0.968438 \text{ Å}^{-1}; \quad \xi_{\text{O}} = 2.143957 \text{ Å}^{-1} \quad (17)$$

Using dynamic charge transfer, the charges  $q_i$  on each atom are calculated by minimizing the electrostatic energy (i.e., the electro negativity equalization condition),<sup>24</sup> subject to the charge neutrality constraint,  $\sum_i q_i = 0$ . This yields a set of linear equations

$$\sum_j V_{ij} s_j = -\chi_i; \quad \sum_j V_{ij} t_j = -1 \quad (18)$$

and charges are obtained using  $\mu = \sum_i s_i / \sum_i t_i$ ;  $q_i = s_i - \mu t_i$ . Because of the functional form of the potential and the way in which the constants are defined, the Streitz–Mintmire potential can be used for Al–O, O–O, and Al–Al interactions. In the

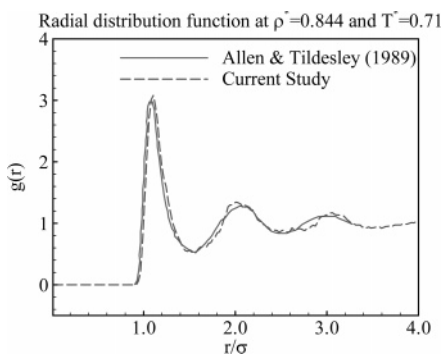


**Figure 3.** Radial distribution functions for liquid argon using NVE simulations.

present study, only Al–Al interactions come into play because only pure aluminum particles are considered.

#### IV. Model Validation

The NVE and NPH algorithms<sup>25</sup> developed in the present study were validated by simulating argon in different (i.e., solid, liquid, and vapor) phases and its thermodynamic transition from the solid to the liquid phase, because of the availability of extensive and reliable experimental data.<sup>25–27</sup> The interatomic interactions were simulated using the Lennard-Jones potential. Melting is identified using the radial-distribution function, translational-order parameter, Lindemann index, and time evolution of the average potential energy. The solid-state simulations predict an equilibrium lattice spacing of 5.26 Å, which matches exactly the values in the literature. The kinetic, potential, and total energies per atom are obtained for the system equilibrated at different random temperatures using both the NVE and NPH ensembles. With the equilibrium pressure from the NVE ensemble as a known condition, calculations were carried out using the NPH ensemble. Identical results were achieved. This was used as a validation tool for the two codes because the microcanonical (NVE) and isobaric–isoenthalpic (NPH) ensembles should be equivalent for calculations of thermodynamic quantities, without sacrificing the dynamical description of the fluid. Extensive validation tests were performed for phase transition. The predicted melting points agree well with the data in the literature. The results also matched those from the molecular-dynamics simulations conducted by Thompson et al.<sup>26</sup> and Solca et al.<sup>25,27</sup> at their respective ambient conditions.

The validation study for the liquid phase was conducted by simulating a liquid droplet of argon in equilibrium with its saturated vapor using the Lennard-Jones potential and NPH ensemble. The average density of the droplet (1200 kg/m<sup>3</sup>) matched the value reported at the saturation temperature in ref 28. Figure 3 shows the radial distribution function of bulk liquid argon at a reduced density ( $\rho\sigma^3$ ) of 0.844 and a reduced temperature of 0.71 ( $k_B T/\epsilon$ ). Excellent agreement was obtained with the result reported in ref 14.

#### V. Melting of Aluminum

After validation, the general framework described in sections II and III was employed to study the melting of nanoscale aluminum particles. Figure 4 shows the melting phenomenon of bulk aluminum in a vacuum. The simulation was performed using the glue potential and periodic boundary conditions. An FCC lattice was adopted to calculate the initial position vectors for the known number of aluminum atoms. Melting is observed at a temperature of 1244 K, at which point sharp variations occur in the potential energy, atomic density, translational-order parameter, radial-distribution function, and the Lindemann index.

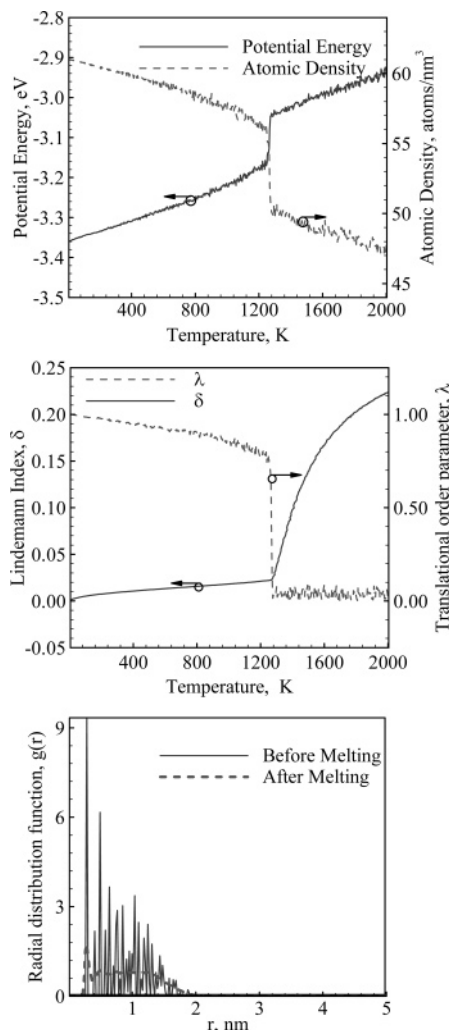


**Figure 4.** Variations of thermodynamic and structural properties during melting of bulk aluminum in vacuum; the glue potential.

The melting of nanoscale aluminum particles was examined in the size range of 2–9 nm. The simulations started with solid phase aluminum using an FCC crystal structure in a cubic configuration. Figure 5 shows the changes in the same thermodynamic and structural properties for a 4 nm particle consisting of 2048 atoms. Melting occurs at 735 K. Since the potential energy and atomic density vary smoothly at the melting point for a particle, only the translational-order parameter and Lindemann index are employed to characterize the melting point for the rest of the study.

The phenomenon of surface premelting represents a qualitative difference between the calculated bulk-material and particle melting. A bulk solid can be simulated by enforcing periodic boundary conditions in all three spatial directions, whereas a particle is associated with a free surface. In the case of a particle, the surface acts as a nucleation site for the phase transition and propagates to the interior. Hence, the phase change in a particle is manifested by a gradual increase in such properties as the potential energy and Lindemann index, as opposed to the abrupt variations found in a bulk material.

Starting with the FCC aluminum in the solid phase, the nanoscale aluminum particle takes on a spherical shape due to surface tension in the liquid phase after melting. A solid-state spherical nanoparticle can be obtained by cooling the liquid aluminum down to a temperature below the melting point, as shown in Figure 6. The density contour can be obtained using the postprocessing code, in which the atoms in the computational

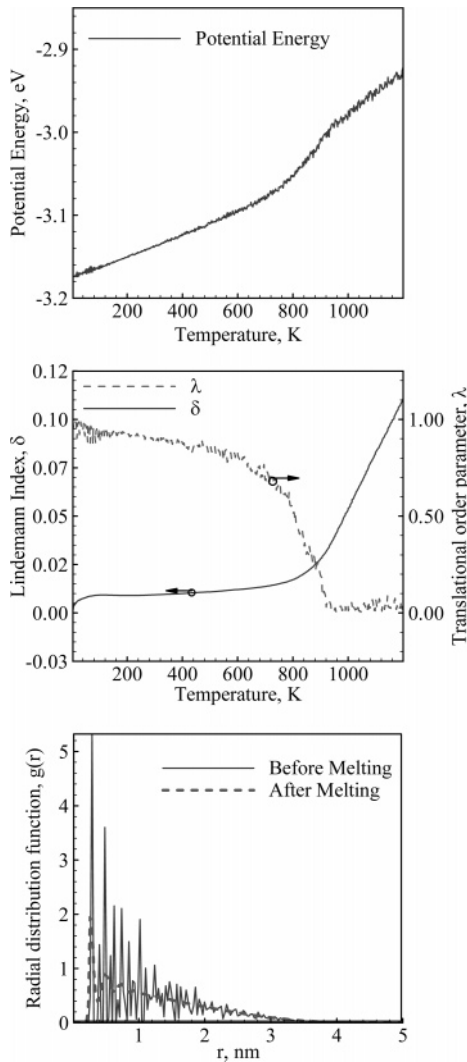


**Figure 5.** Variations of thermodynamic and structural properties during melting of nanoscale aluminum particle,  $d_p = 4$  nm; the glue potential.

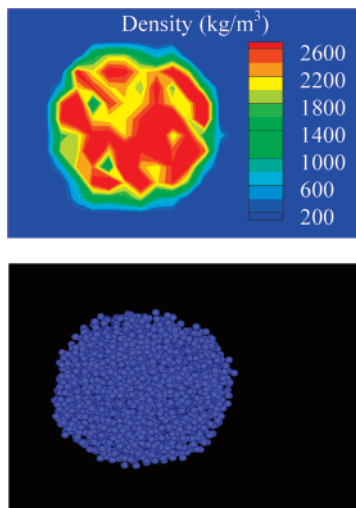


**Figure 6.** A 4 nm aluminum particle in solid state; the glue potential.

domain are mapped on a grid and the thermodynamic properties like density are calculated by averaging the properties in all of the cells. The result agrees closely with the density of solid-state aluminum of  $2700 \text{ kg/m}^3$ , further validating the simulations.

The calculations using the five potentials were also checked against the cohesive energies of bulk aluminum in the solid state

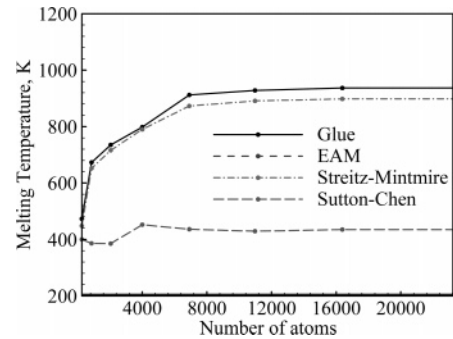


**Figure 7.** Melting point of nanoscale aluminum particle as function of particle size.

**TABLE 1: Cohesive Energies for Bulk Aluminum**

potential	calculated (eV)	literature (eV)
Lennard-Jones Potential	-3.353	
glue potential	-3.360	-3.360 <sup>20</sup>
embedded atom potential	-3.385	
Streitz-Mintmire potential	-3.385	-3.390 <sup>18</sup>
Sutton-Chen potential	-3.312	-3.340 <sup>22</sup>

using the microcanonical ensemble. Table 1 shows the comparison of cohesive energies obtained in the current study with those reported in the literature. The calculated energies match exactly the values found in the literature.

The effect of particle size on melting in vacuum was investigated. Figure 7 shows the results using isobaric-isenthalpic ensembles based on five different potentials. The corresponding numerical values are listed in Table 2. The melting temperature increases from 473 K for a 2 nm particle and reaches the bulk value of 937 K for 8 nm and larger-sized particles. Annealing was accomplished with the velocity scaling at a rate of 0.01 K per step. The results obtained in the present study bear a close resemblance to the experimental data of Eckert et al.<sup>6</sup> but cannot be compared quantitatively because of the absence of oxide layer in the simulations.

The two-body Lennard-Jones potential failed to predict the melting point for nanoscale aluminum particles. Even at 1200 K, the particle still remains in the solid state, and only an increase in the vibrational frequency was observed. A similar phenomenon was noted in the simulations for bulk aluminum. The Sutton-Chen potential was found to predict geometrical structures for nano clusters very accurately<sup>4</sup> but failed to provide an accurate prediction of the melting point for nanoscale aluminum particles. This is an example where a potential fitted to structural properties like elastic constants and bulk modulus fails to perform well for thermodynamic properties. The glue and Streitz-Mintmire potentials are comparable. The former generally leads to a melting temperature about 50–100 K higher than the latter does. The success of the glue and Streitz-Mintmire potentials in capturing the effect of size on melting of nanosized aluminum particles once again underlines the importance of many-body potentials for modeling aluminum behavior.

The glue and Streitz-Mintmire potential predict bulk melting points of 1244 and 1146 K, respectively, which are greater than the thermodynamic melting point by about 18%. According to the study by Lutsko et al.<sup>29</sup> a factor should be introduced between the simulated (structural) and the actual (thermodynamic) melting points when periodic boundary conditions are enforced for bulk materials. The thermodynamic melting point is approximately 0.75–0.85 times its structural counterpart.<sup>29</sup> Applying this factor to obtain the predicted thermodynamic melting point gives a value close to 940 K for bulk aluminum.

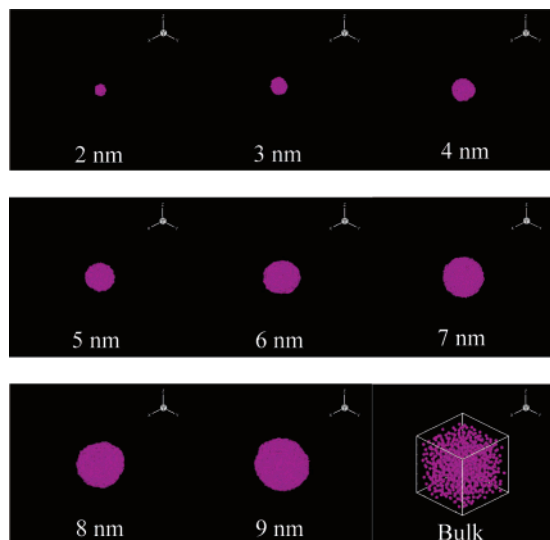
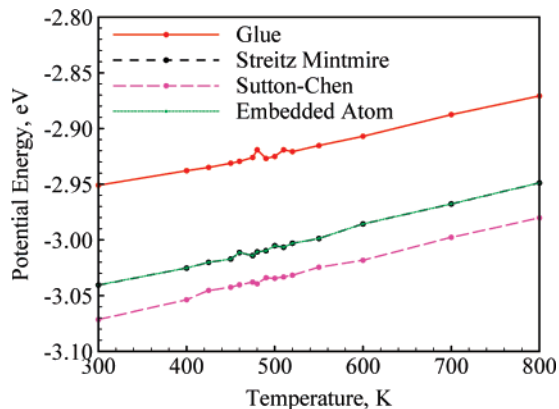


**Figure 8.** Spherical shape assumed by nanoscale aluminum particles after melting.

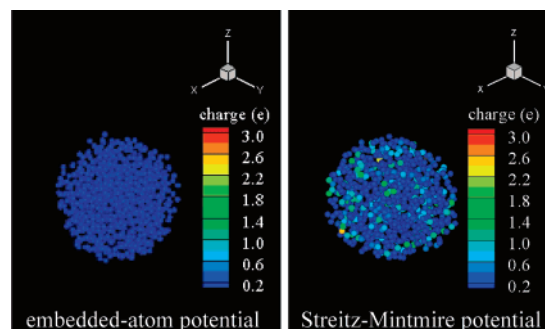
Since, in the case of particles, the free surface acts as a nucleation site for melting, the phase change predicted by NPH simulations directly corresponds to the thermodynamic melting and no correction factor is required.

Figure 8 shows final spherical shapes attained by aluminum nanoparticles in the size range of 2–9 nm at 1200 K as a result of surface tension. All of the simulations commenced with cubic geometries and were based on the glue potential.

In all of the simulations discussed above, the aluminum temperature was increased continuously by means of velocity scaling, and melting was identified based on the variations in the structural and thermodynamic properties. The procedure amounts to the heating of a solid material in vacuum until the transition to a liquid state is achieved. For particles containing 500 atoms or less, uncertainties arise in characterizing the phase transition due to the coexistence of the solid and liquid phases. An alternative approach to obtain the melting point is thus implemented by equilibrating the particle at specific temperatures and calculating the thermodynamic and structural properties for each respective state. The method is more appropriate for small clusters, although it is computationally more expensive. Figure 9 shows the results for a 2 nm particle (256 atoms) from such equilibrium simulations in terms of the variation of potential energy as a function of temperature. The melting was characterized by fluctuations in the potential energy, a phenomenon referred to as dynamic melting by Alavi et al.<sup>4</sup> The particle oscillates between the liquid and solid phases in the temperature range of 450–475 K, as evidenced by the fluctuations in potential energy. As in the previous simulations, the Lennard-Jones and Sutton–Chen potentials could not predict the dynamic melting behavior accurately. The glue and Streitz–Mintmire potentials, although they produce different magnitudes of equilibrium potential energy, result in the same temperature range for dynamic melting.



**Figure 9.** Variation of equilibrium potential energy with temperature for 2 nm sized particle (256 atoms).



**Figure 10.** Surface charge development for 3 nm aluminum particle using the embedded-atom and Streitz–Mintmire potentials.

The effect of surface charges on the melting of a nanoparticle also needs to be investigated, although this phenomenon is often negligible for a bulk material due to the lack of surface. To this end, the results of simulations performed for nanoparticles in the range of 2–9 nm, using the embedded-atom and Streitz–Mintmire potentials, were analyzed. The two potentials are identical except that the former ignores completely the electrostatic part of the latter. The development of surface charges for 2–9 nm particles appears to be too small to exert a significant influence on the electrostatic part of the Streitz–Mintmire potential, and both potentials result in exactly the same melting point. A similar observation was reported by Alavi et al. based on a simulation of 500 aluminum atoms in an FCC structure.<sup>30</sup> Figure 10 shows the final spherical shape with charges for a 3 nm nanoparticle. For particles smaller than 3 nm, the surface charge development plays a negligible role in determining the dynamic melting behavior as well and the results are identical to those from embedded-atom potential.

## VI. Summary and Conclusions

Molecular-dynamics simulations using isobaric–isoenthalpic (NPH) ensembles have been performed to characterize the melting of nanosized aluminum particles in the range of 2–9 nm and to investigate the effect of surface charge development

**TABLE 2: Melting Points of Nanoscale Aluminum Particles as Function of Particle Diameter**

potentials	particle size (atoms)								
	2 nm (256)	3 nm (864)	4 nm (2048)	5 nm (4000)	6 nm (6912)	7 nm (10976)	8 nm (16384)	9 nm (23328)	bulk (pbc)
Lennard-Jones									
glue	473	673	735	798	912	928	937	937	1244
embedded-atom	448	652	716	790	873	891	898	898	1146
Streitz–Mintmire	448	652	716	790	873	891	898	898	1146
Sutton–Chen	400	386	385	452	436	429	435	435	529

on melting. Five different potentials were implemented. The two-body Lennard-Jones potential failed to predict the melting point. The Sutton–Chen potential, validated against structural properties, also led to erroneous results of the melting phenomenon. The glue and Streitz–Mintmire potentials predicted accurately the size dependence of the melting temperature, but the former generally yielded a melting temperature about 50–100 K higher than the latter did. The difference in the melting behavior between a nanoparticle and a bulk material was investigated. Sharp variations in structural and thermodynamic properties were found across the melting point for a bulk material. In contrast, only smooth changes were observed for nanoparticles, due to the presence of surface premelting. The melting temperature of an aluminum particle increases monotonically from 473 K at 2 nm to the bulk value of 937 K at approximately 8 nm. As the size decreases below a critical value, the increased surface-to-volume ratio and associated higher surface energy enhanced vibrational instability. This interface-induced disorder is responsible for the size dependence of particles melting at nano scales. For particle sizes less than 3 nm, the solid and liquid phases were found to coexist. The effect of surface charge development on melting was also explored by analyzing the results from the embedded-atom and Streitz–Mintmire potentials. The two potentials are identical except that the former ignores completely the electrostatic part of the latter. The development of surface charges had negligible effect on the particle melting characteristics.

**Acknowledgment.** This work was sponsored by the U.S. Army Research Office under the Multi-University Research Initiative under Contract No. W911NF-04-1-0178. The support and encouragement provided by Drs. David Mann, Kevin L. McNesby, and Ralph Anthenien are gratefully acknowledged.

## Nomenclature

$A$  = surface area  
 $Al$  = aluminum  
 $Al_2O_3$  = aluminum oxide  
 $c$  = specific heat  
 $d_i$  = scaled coordinates  
 $\delta$  = thickness, Lindemann index  
 $\epsilon$  = epsilon (constant for LJ potential)  
 $F_i$  = force  
 $k_B$  = Boltzmann's constant  
 $k$  = conductivity  
 $K$  = kinetic energy  
 $\kappa$  = lattice vector  
 $L$  = Lagrangian  
 $\lambda$  = translational order parameter  
 $\Gamma$  = phase space  
 $m, M$  = mass

$P$  = pressure  
 $q_i$  = scaled coordinates  
 $r, R$  = radius  
 $r_i$  = Cartesian coordinates  
 $r_{ij}$  = distance between two atoms  
 $\rho$  = density  
 $\sigma$  = sigma (constant for LJ potential)  
 $T$  = temperature  
 $t$  = time  
 $U$  = potential energy  
 $V$  = volume

## References and Notes

- (1) Ilyin, A. P.; Gromov, A. A.; Vereshchagin, V. I.; Popenko, E. M.; Surgin, V. A.; Lehn, H. *Combust. Expl. Shock Waves* **2001**, *37*, 664.
- (2) Kwon, Y. S.; Gromov, A. A.; Ilyin, A. P.; Popenko, E. M.; Rim, G. H. *Combust. Flame* **2003**, *133*, 385.
- (3) Pivkina, A.; Ulyanova, P.; Frolov, Y.; Zavyalov, S.; Schoonman, J. *Prop. Explos. Pyrotech.* **2004**, *29*, 39.
- (4) Alavi, S.; Thompson, D. L. *J. Phys. Chem. A* **2006**, *110*, 1518.
- (5) Wronski, C. R. M. *Brit. J. Appl. Phys.* **1967**, *18*, 1731.
- (6) Eckert, J.; Holzer, J. C.; Ahn, C. C.; Fu, Z.; Johnson, W. L. *Nanostruct. Mater.* **1993**, *2*, 407.
- (7) Bucher, P.; Yetter, R. A.; Dryer, F. L.; Vicenzi, E. P.; Parr, T. P.; Hanson, D. M. *Solid Propellant Chemistry, Combustion and Motor Interior Ballistics. Prog. Astronaut. Aeronaut.* **2000**, *185*, 689.
- (8) Rai, A.; Lee, D.; Park, K.; Zachariah, M. R. *J. Phys. Chem. B* **2004**, *108*, 14793.
- (9) Rozenband, V. I.; Vaganova, N. I. *Combust. Flame* **1992**, *88*, 113.
- (10) Dreizin, E. L. *Combust. Expl. Shock Waves* **2003**, *39*, 681.
- (11) Trunov, M. A.; Schoenitz, M.; Dreizin, E. L. *Combust. Theory Model.* **2006**, *10*, 603.
- (12) Campbell, T. J.; Aral, G.; Ogata, S.; Kalia, R. K.; Nakano, A.; Vashishta, P. *Phys. Rev. B* **2005**, *71*, 205413.
- (13) Anderson, H. C. *J. Chem. Phys.* **1980**, *72*, 2384.
- (14) Allen, M. P.; Tildesley, D. J. *Computer Simulation of Liquids*; Oxford Science: Oxford, 1989.
- (15) Zhou, Y.; Karplus, M.; Ball, K. D.; Berry, R. S. *J. Chem. Phys.* **2002**, *116*, 2323.
- (16) Gezelter, J. D.; Rabani, E.; Berne, B. J. *J. Chem. Phys.* **1997**, *107*, 4618.
- (17) Plimpton, S. J. *Comput. Phys.* **1995**, *117*, 1.
- (18) Streitz, F. H.; Mintmire, J. W. *Phys. Rev. B* **1994**, *50*, 11996.
- (19) Halicioglu, T.; Pound, G. M. *Phys. Status Solidi A* **1975**, *30*.
- (20) Ercolessi, F.; Adams, J. B. *Europhys. Lett.* **1994**, *26*, 583.
- (21) Joswig, J. O.; Springborg, M. *Phys. Rev. B* **2003**, *68*, 085408.
- (22) Sutton, A. P.; Chen, J. *Philos. Mag. Lett.* **1990**, *61*, 139.
- (23) Roohtan, C. C. J. *J. Chem. Phys.* **1951**, *19*, 1445.
- (24) Rappe, A. K.; Goddard, W. A. *J. Phys. Chem.* **1991**, *95*, 3358.
- (25) Solca, J.; Anthony, J. D.; Steinebrunner, G.; Kirchner, B.; Huber, H. *J. Chem. Phys.* **1997**, *224*, 253.
- (26) Agarwal, P. M.; Rice, B. M.; Thompson, D. L. *J. Chem. Phys.* **2003**, *118*, 9680.
- (27) Solca, J.; Dyson, A. J.; Steinebrunner, G.; Kirchner, B.; Huber, H. *J. Chem. Phys.* **1998**, *108*, 4107.
- (28) Little, J. K. Ph.D. Dissertation. Department of Mechanical Engineering, The Pennsylvania State University: PA, 1996.
- (29) Lutsko, J. F.; Wolf, D.; Phillipot, S. R.; Yip, S. *Phys. Rev. B* **1989**, *40*, 2841.
- (30) Alavi, S.; Mintmire, J. W.; Thompson, D. L. *J. Phys. Chem. B* **2005**, *109*, 209.